A Method for Correcting Staggered Pulse Repetition Time (PRT) and Dual Pulse Repetition Frequency (PRF) Processor Errors in Research Radar Datasets

A. Addison Alford,[a,b] Michael I. Biggerstaff,[a,c,d] Conrad L. Ziegler,[b,c] David P. Jorgensen,[b,c] and Gordon D. Carrie[c]

[a] *Cooperative Institute for Severe and High-Impact Weather Research and Operations, University of Oklahoma, Norman, Oklahoma*
[b] *National Severe Storms Laboratory, National Oceanic and Atmospheric Administration, Norman, Oklahoma*
[c] *School of Meteorology, University of Oklahoma, Norman, Oklahoma*
[d] *Advanced Radar Research Center, University of Oklahoma, Norman, Oklahoma*

ABSTRACT: Mobile weather radars at high frequencies (C, X, K, and W bands) often collect data using staggered pulse repetition time (PRT) or dual pulse repetition frequency (PRF) modes to extend the effective Nyquist velocity and mitigate velocity aliasing while maintaining a useful maximum unambiguous range. These processing modes produce widely dispersed "processor" dealiasing errors in radial velocity estimates. The errors can also occur in clusters in high shear areas. Removing these errors prior to quantitative analysis requires tedious manual editing and often produces "holes" or regions of missing data in high signal-to-noise areas. Here, data from three mobile weather radars were used to show that the staggered PRT errors are related to a summation of the two Nyquist velocities associated with each of the PRTs. Using observations taken during a mature mesoscale convective system, a landfalling tropical cyclone, and a tornadic supercell storm, an algorithm to automatically identify and correct staggered PRT processor errors has been developed and tested. The algorithm creates a smooth profile of Doppler velocities using a Savitzky–Golay filter independently in radius and azimuth and then combined. Errors are easily identified by comparing the velocity at each range gate to its smoothed counterpart and corrected based on specific error characteristics. The method improves past dual PRF correction methods that were less successful at correcting "grouped" errors. Given the success of the technique across low, moderate, and high radial shear regimes, the new method should improve research radar analyses by affording the ability to retain as much data as possible rather than manually or objectively removing erroneous velocities.

KEYWORDS: Algorithms; Data quality control; Radars/Radar observations; Weather radar signal processing

1. Introduction

The maximum unambiguous range of a weather radar is proportional to the pulse repetition time (PRT) while the maximum unambiguous (or Nyquist) velocity is inversely proportional to the PRT. Hence, weather radar cannot simultaneously maximize both the distance sampled and the span of unambiguous radial velocities. This condition has been referred to as the Doppler dilemma (Atlas et al. 1963). In situations where the true wind velocity exceeds the maximum unambiguous velocity, extending the Nyquist interval will reduce the degree of velocity aliasing that must be corrected either objectively (James and Houze 2001; Helmus and Collis 2016) or subjectively (e.g., Oye et al. 1995). However, increasing the Nyquist interval can enhance the potential for range ambiguities, which may overlap and contaminate first-trip signals (Zrnić and Mahapatra 1985). In operational and research applications, rigorous postprocessing of radar data must be performed to conduct range unfolding and remove range overlaid echoes and to dealias radial velocities for use in numerical weather prediction models (Montmerle and Faccani 2009; Dong and Xue 2013; Shen et al. 2016), observational analysis such as dual and multi-Doppler wind syntheses (Biggerstaff and Houze 1991; Palucki et al. 2011; DiGangi et al. 2016; Betten et al. 2018; Alford et al. 2019a,b, 2020), and severe weather detection (Mitchell et al. 1998; Joe et al. 2004; Smith et al. 2016).

Techniques to mitigate the effects of the Doppler dilemma (Sirmans et al. 1976; Dazhang et al. 1984) have been employed in operational networks such as the U.S. WSR-88Ds (Crum and Alberty 1993; Doviak et al. 2000) and research mobile radars such as the Shared Mobile Atmospheric Research and Teaching (SMART) radars (Biggerstaff et al. 2005) and the Doppler on Wheels (DOW) radars (Wurman et al. 2007), as well as the vertically scanning radar on the NOAA P-3 aircraft (Jorgensen et al. 1983). The mitigation methods fall into two categories, those that maintain the maximum unambiguous range while increasing the effective Nyquist velocity [dual pulse repetition frequency (PRF); Dazhang et al. 1984; and staggered PRT modes; Sirmans et al. 1976] and those that maintain the Nyquist velocity while increasing the maximum unambiguous range (random phase signal processing; Zrnić and Mahapatra 1985). Here, we focus on the first category.

In the dual PRF method, two uniform time series are collected sequentially at different PRTs to produce a single ray of data. Velocities (or lag-1 autocorrelation phases) derived from each time series are combined to obtain a new (dealiased)

Jorgensen: Retired.

Corresponding author: A. Addison Alford, addison.alford@noaa.gov

velocity estimate with a corresponding larger maximum unambiguous velocity. Hence, there is an inherent requirement of spatial continuity over the combined interval during which the two time series are collected. Thus, for mechanically scanning radars, regions of high shear are prone to error in the estimate of radial velocity (Joe and May 2003; Altube et al. 2017). The error rates also generally increase with increasing antenna rotation rate. In the staggered PRT method, the PRT is changed between pulses to produce a nonuniform time series from which a ray of data is created. The advantage of the staggered method is that the radar can be operated at a faster rotation rate without penalty, since spatial continuity is less of a concern (Holleman and Beekhuis 2003).

Both dual PRF and staggered PRT velocity dealiasing methods are similar and are described here following the Vaisala (2014, 2017) implementation that discusses the maximum unambiguous velocity extension technique in terms of lag-1 autocorrelation phases. The process is similar to that discussed in other dual PRF and staggered PRT studies. The dual PRF and staggered PRT techniques are similar in that a new phase angle is created from the difference between the phase angle at high and low PRTs. The new phase angle has an extended Nyquist velocity relative to that from either PRT, but has twice the phase noise (i.e., the variance of the measured phase) since it contains information from both the measured high and low PRT lag-1 autocorrelation phases. Rather than use the noisy new phase angle directly, the algorithms use the new velocity estimate as a constraint to select the closest solution from projections of the single PRT velocity mapped into the new phase space (Vaisala 2014, 2017). In the dual PRF method, the dealiased phase shift from the prior time series is used in the projection to dealias the current time series velocity lag-1 estimate.

There exist two methods of implementing staggered PRT, where the first relies on the difference between the two phase angles of the autocorrelation function from samples at both PRTs (Zrnić and Mahapatra 1985). Due to the combination of the phase noise, this method yields Doppler velocity errors similar to those described in dual PRF processing (e.g., Fig. 1). However, a technique to correct them in postprocessing does not exist to our knowledge. The method is implemented in many research radars and is detailed more in section 2. The second method is implemented in U.S. National Weather Service WSR-88D radar processors in real time. The application of the staggered PRT method (Torres et al. 2004) is optimized for operational use including the minimization of errors but is not implemented in most research radars. Specifically, the WSR-88D staggered PRT dealiasing uses a velocity difference transfer function to extend the observable maximum unambiguous Doppler velocity. For a given staggered PRT ratio, a table of rules that optimally reduces staggered PRT errors is precomputed. Based on minimizing the velocity difference transfer function, the appropriate Nyquist interval is added to the Doppler velocity measured at the low PRT. The rules (in addition to other quality control steps taken) are implemented on board the WSR-88D signal processor. Theoretically, the method could be applied on board research radar signal processors but would require modification by the

manufacturers for implementation. In postprocessing, the necessary information (e.g., knowledge of the Doppler velocity information sampled at both PRTs) that is needed to apply the Torres et al. (2004) method is often not retained by most research radars. Thus, the method is not applicable to datasets collected previously that do not retain the necessary information. Because most research radars utilize the former Zrnić and Mahapatra (1985) method and do not retain the necessary information to implement the Torres et al. (2004) method, we focus *solely* on the former method in this manuscript.

Errors in the dual PRF technique are characterized as generally localized points surrounded by accurate estimates of radial velocity (Jorgensen et al. 2000; May 2001). They have been found to occur especially in regions of high azimuthal wind shear. Joe and May (2003) noted that an erroneous estimate of true radial velocity (V_{True}) was likely when the Doppler velocity being dealiased (V_2) was sufficiently larger than the Doppler velocity at the adjacent gate (V_1) in the previous ray. The error condition is provided by the expression

$$\left| \frac{V_2 T_2 - V_1 T_1}{T_2 - T_1} - V_2 \right| > V_{N2}, \tag{1}$$

where V_{N2} is the Nyquist velocity using a PRT of T_2 and V_1 is the Doppler velocity in the previous ray that was sampled at a PRT of T_1. Note that for dual PRF processing, PRTs are selected in specific ratios such as $(m+1)T_2/mT_1$, where m typically is 2, 3, or 4.

Rather than remove the Doppler velocities at gates in which an error has occurred (here often referred to as "processor errors"), processor errors are corrected postarchive by adding or subtracting even multiples of either the low or high Nyquist velocity to minimize the difference of the estimate of V_{True} relative to the surrounding velocities. Various algorithms exist to correct dual PRF processor errors (Joe and May 2003; Holleman and Beekhuis 2003; Altube et al. 2017). The method of Joe and May (2003) identifies a radial velocity point as an error by using the mean velocities of the surrounding points. Their correction scheme does not necessarily rely on previous knowledge of the PRF in each ray, making it useful for automated processing of data from different radars. The Holleman and Beekhuis (2003) technique takes a statistical approach to identify the PRF for each ray and provides a robust correction for errors using the deviation of points from their local median velocity and adding or subtracting the proper Nyquist interval. Alternatively, Altube et al. (2017) use circular statistics in phase space rather than velocity space to identify and correct dual PRF errors. However, knowledge of the PRF in each ray is required.

We know of no technique to identify and correct velocity errors associated with the staggered PRT signal processing mode as applied through the Zrnić and Mahapatra (1985) method that is discussed here. Speckled velocity errors found in dual PRF processing are similarly seen in staggered PRT data (Torres et al. 2004; Tabary et al. 2005) analogous to those described in the dual PRF mode by Joe and May (2003), Holleman and Beekhuis (2003), and Altube et al. (2017).
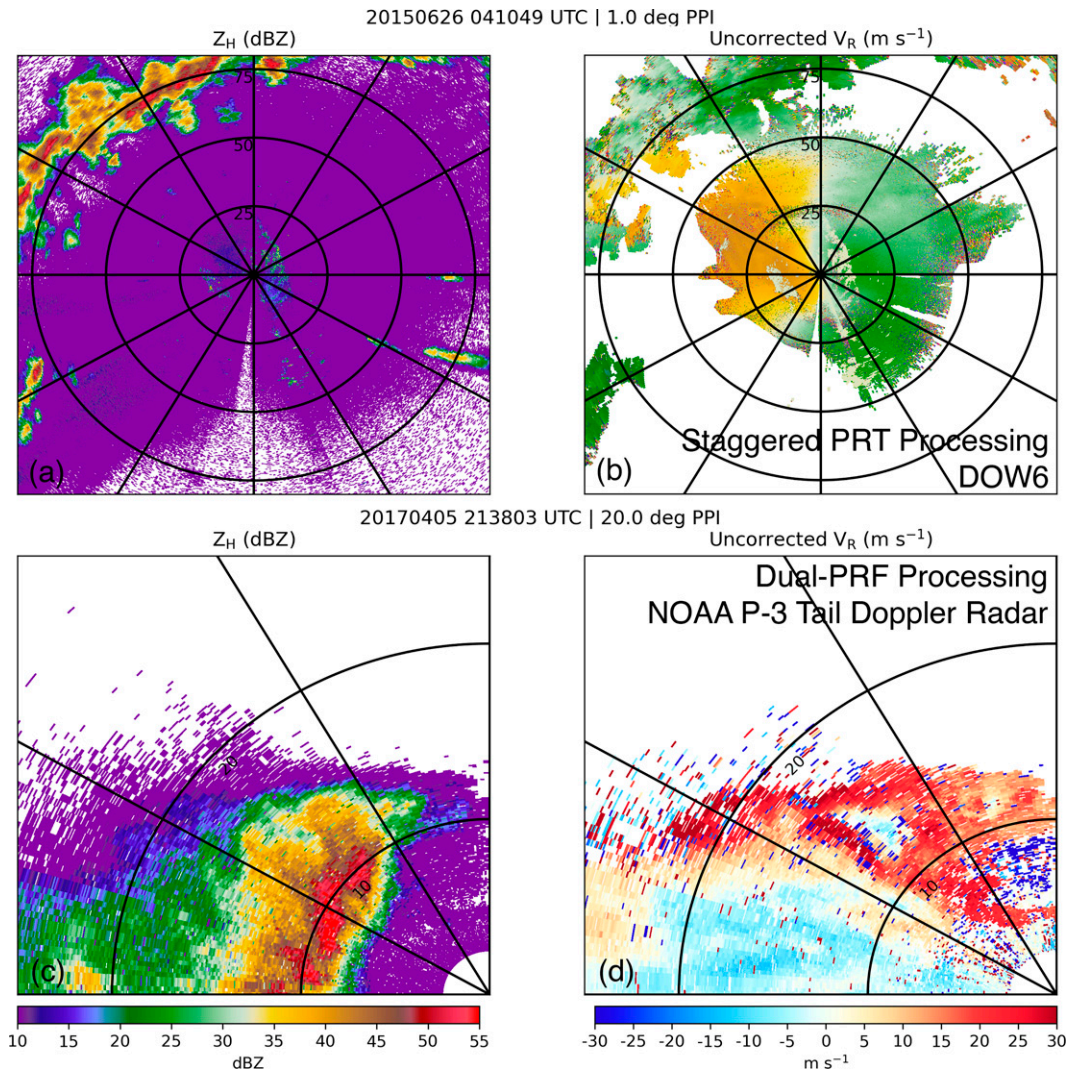
FIG. 1. (a) Radar reflectivity, in dBZ according to the color scale, and (b) unedited staggered PRT Doppler velocities at 1.0° elevation angle from the DOW6 mobile radar at 0410:49 UTC 26 Jun 2015 obtained during PECAN. (c) Radar reflectivity, in dBZ according to the color scale, and (d) unedited dual PRF Doppler velocities from the vertically scanning NOAA P-3 aircraft tail Doppler radar collected at 2138:03 UTC 5 Apr 2017 during VORTEX-SE. All plan position indicators (PPIs) are shown in polar coordinates with the range rings distances indicated (in km) and azimuth every 30°.

However, since the staggered PRT method averages both high and low PRT velocity estimates (discussed further in section 2), the error characteristics differ from the dual PRF processing modes. More importantly, the standard dual PRF correction technique that adds or subtracts multiples of a single PRT Nyquist velocity would not apply to the staggered PRT processor errors. In practice, staggered PRT processor errors are most often removed in postprocessing rather than corrected, creating data void speckles in regions with generally high signal-to-noise ratio. In the past, removal required tedious manual editing of the data before research quality analyses could be conducted. A large body of previously collected research radar data containing processor errors from dual PRF and staggered PRT modes exists. Hence,

a robust technique to correct errors in a staggered PRT framework is needed by the research community.

Here a simple but robust method for identifying and correcting staggered PRT processing velocity errors is presented and evaluated for different types of convective storms using data from mobile weather radars. In contrast to previous dual PRF methods, it is shown here that using a Savitzky–Golay-based method is more robust in correcting errors than a two-dimensional, median filter pass through the data. The filter method is especially useful for regions of high shear, along the edges of storm echoes, and grouped errors where 3 × 3 window methods tend to perform the worst. In staggered PRT processing, the intraray change in the PRF is uniform for all rays, simplifying the identification and correction of

velocity errors. In some dual PRF velocity error algorithms, knowledge of the interray PRF information is required (Altube et al. 2017). Yet, we also show that the same framework can be applied to dual PRF errors without knowledge of the interray PRF information.

2. Characterization of staggered PRT errors

Since the estimates of the Doppler velocities at the low and high PRFs are sampled in nearly the same physical space when the staggered PRT method is employed, the staggered PRT method should be less prone to errors due to extreme shear as compared to the dual PRF method. However, as shown in Fig. 1b, obvious errors still exist in regions of strong shear and clear air. It is likely that large spectrum width in regions of radial velocity shear or low signal-to-noise ratio in regions of clear-air return could yield sufficient error in the Doppler velocity estimates V_2 and V_1 such that the independent dealiasing of each Doppler velocity estimate incurs an error. Similar to dual PRF, V_2 and V_1 are the Doppler velocities taken at the high and low (or low and high) PRF pulses. The order is not important to the technique.

In this summary of the staggered PRT technique, we examine the specific technique discussed by Zrnić and Mahapatra (1985) and Vaisala (2014, 2017) where both Doppler velocity samples collected at each PRT are dealiased using one another and then averaged together. This method is not to be confused with the velocity transfer function method described in Torres et al. (2004), although the following method is indeed summarized in Torres et al. as well. In staggered PRT mode, dealiasing radial velocity measurement V_2 requires an initial estimate of the correct velocity (V_C) that is determined from Eq. (2) where λ is the wavelength of the radar, $\theta_{1,2}$ is the phase of the lag-1 autocorrelation function from the high and low PRT pulses (Zrnić and Mahapatra 1985; Doviak and Zrnić 2006; Vaisala 2014, 2017), and $T_{1,2}$ is as in Eq. (1):

$$V_C = \frac{\lambda(\theta_2 - \theta_1)}{4\pi(T_2 - T_1)}. \tag{2}$$

As discussed previously, the ratio of T_2 to T_1 (written here where $T_2 > T_1$, but may be interchanged) follows $(m + 1)T_2/mT_1$, where m is 2, 3, or 4. As noted above, this estimate of V_C is not used directly due to the addition of phase noise from each phase shift measurement (Holleman and Beekhuis 2003). We also note that the difference in phase angles must lie between $-\pi$ and π as described in Torres et al. (2004). The estimate of dealiased V_2 ($V_{2\text{True}}$) is derived by selecting the integer n such that

$$|V_c - V_2 - 2nV_{N2}| < V_{N2}, \tag{3}$$

where V_{N2} is the Nyquist velocity at PRT$_2$. Once n is selected, $V_{2\text{True}}$ is determined using Eq. (4):

$$V_{2\text{True}} = V_2 + 2nV_{N2}. \tag{4}$$

Independently, V_1 is also dealiased in the same manner. The staggered PRT mode as applied here averages together the $V_{1\text{true}}$ and $V_{2\text{true}}$ values to arrive at the recorded velocity.

Following Eqs. (2)–(4), the mean estimate is shown in Eq. (5) where n_2 and n_1 are the integers calculated as in Eq. (3) but for each independent dealiasing of V_2 and V_1:

$$V_{\text{Avg}} = \frac{(V_2 + 2n_2V_{N2}) + (V_1 + 2n_1V_{N1})}{2}. \tag{5}$$

Thus, we consider error characteristics to be of the general form

$$\text{error} = dn_2V_{N2} + dn_1V_{N1}, \tag{6}$$

where dn_2 and dn_1 represent the error associated with selecting the incorrect n_2 and n_1. Most often, we find that a velocity error produced in the staggered PRT method would have a magnitude $\pm(dn_2V_{N2} + dn_1V_{N1})$ (where dn_1, $dn_2 = 0, 1, 2, 3, \ldots$).

3. Correction method

In previous studies that focused on dual PRF corrections (Holleman and Beekhuis 2003; Joe and May 2003; Altube et al. 2017), a two-dimensional 3×3 (i.e., three gates in the radial and azimuthal directions, respectively, centered on the gate being examined) moving window was used to assess the background velocity and identify outliers that were improperly dealiased by the radar signal processor. Applying two-dimensional approaches to the staggered PRT data examined here led to a large number of remaining processor errors, particularly in regions where the velocity errors are numerous (Fig. 2). In brief, we attempted to modify the median-based 3×3 window approaches such as those in Holleman and Beekhuis (2003), but apply the appropriate correction for staggered PRT velocity errors. While met with success in regions of randomly distributed velocity errors, groups of incorrect velocities can also be seen in both cases that are left and result where the error identification mistakes processor errors for locally correct velocities. Enlarging the windows can help on the edges of precipitation in data-sparse regions, but often fail in regions of intense radial and azimuthal shear where velocity errors tend to be grouped. In a growing mesoscale convective system (Figs. 1a,b, 2a,b), for example, the shear between growing convective cells can lead to rapid changes in the Doppler velocities and can lead to numerous velocity errors in a small area. To mitigate the issue, we attempted a 5×5 window (larger than most dual PRF algorithms; not shown) and were met with similar results. Hence, the 5×5 window was likely too large to identify a useful background flow given the variability of the flow characteristics in azimuth and range within the window.

Rather than employ the above median-filtering-based methods, the correction method presented here is based on comparing the recorded Doppler velocities to a filtered Doppler velocity field on a gate-by-gate basis. The algorithm then uses numerical characteristics of the difference between the filtered and raw Doppler velocities to identify errors. Assuming that the filtered velocity field locally approximates the true velocity field, the velocities that differ by more than $\pm(n_2V_{N2} + n_1V_{N1})$
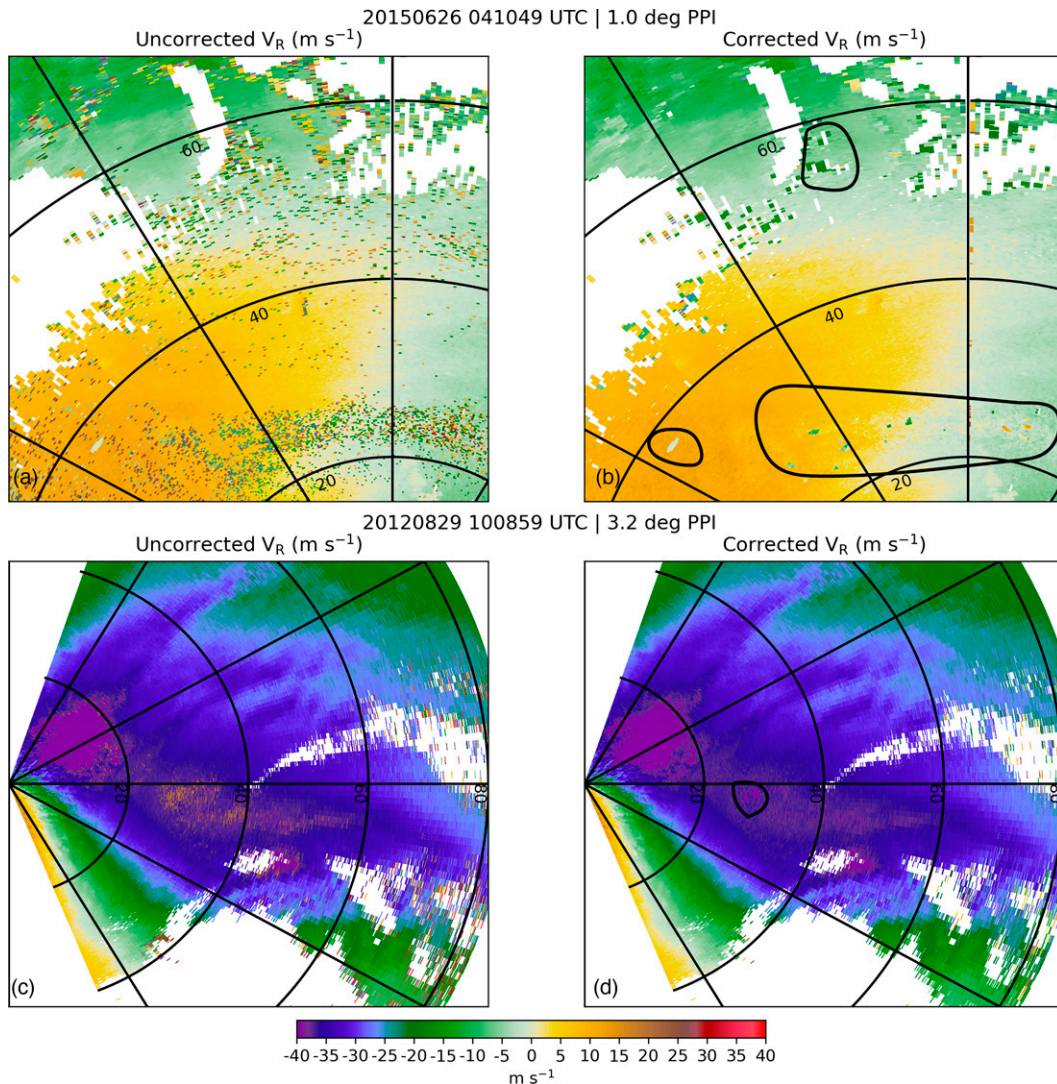
FIG. 2. (a) Uncorrected radial velocities in a developing mesoscale convective system are shown. (b) The radial velocities corrected by a two-dimensional window method associated with dual PRF correction algorithms (e.g., Holleman and Beekhuis 2003). (c),(d) As in (a) and (b), but for a landfalling tropical cyclone. The black outlines highlight regions of grouped errors that remain after correction.

(where n_1 and $n_2 = 0, 1, 2, 3, \ldots$ and omitting $n_1 = n_2 = 0$) from the filtered velocities are corrected.

a. Algorithm description

The algorithm identifies errors by comparing the collected Doppler velocity field to a combined filtered field. To create the filtered field, each recorded azimuth of data is independently linearly interpolated to fill locations of missing data. This is done to assure data are available near the edges of the data field. Linear interpolation as applied here does not change the Doppler velocities, rather only linearly interpolates in areas of missing data along the ray or azimuth. The linearly interpolated data are then passed through a Savitzky–Golay filter (hereafter "SGF"; Savitzky and Golay 1964) using a radial (azimuthal) window of 11 (5) gates. The

SGF is designed to remove noise in a signal via a local, running least squares fit to the data within some window. Specifically, each group of points within the window is fit to some curve (in this case, a cubic polynomial) using least squares minimization between the observed points in the window and the fitted curve. For additional details, the reader is referred to appendix I of Savitzky and Golay (1964). In the present application, the filter smooths to suppress the velocity errors while retaining the general, local character of the true flow. The radial and azimuthal filtered fields are retained and a third field is created by averaging the two (the mean filtered field). Three "difference fields" are created by subtracting the filtered fields from the original Doppler velocities: a difference field using the SGF-radial filter (the radial difference field), the SGF-azimuthal filter (the azimuthal difference

field), and a difference field using the mean filtered field (the mean difference field). The mean difference field is then examined to find velocities that are near the possible errors according to Eq. (6).

To identify staggered PRT errors, gates with difference values δ near 0 m s^{-1} are considered the truth. In essence, this implies that the recorded Doppler velocity is similar to other velocities in the vicinity and is likely accurate. To assure that correct velocities are not considered for error correction, a normal distribution is initially fit to the radial and azimuthal difference fields independently and used to determine which velocities to consider for correction. In our Python-based algorithm, we employ the normal distribution fit available from the SciPy package (available online at https://scipy.org) that uses the "maximum likelihood estimate" method to retrieve the normal distribution parameters (e.g., the mean and the standard deviation). While the mean difference field is ultimately used in error identification, we initially limit the velocities that are considered for correction by examining the individual radial and azimuthal difference fields first. Velocities in the mean difference field are only considered for correction where their respective radial (azimuthal) difference field value is greater than ± 3 times the standard deviation of the radial (azimuthal) normal distribution. A choice of three standard deviations ensures that only velocities that are truly different than the local flow (i.e., the top 0.3%) are considered for correction. Selecting a lower standard deviation tended to result in some velocities that were aliased into the incorrect interval. However, scenarios in which the Nyquist velocities are small but the standard deviation of the distribution is large, we found a smaller interval may be required. Hence, the three standard deviation criterion is replaced with the low Nyquist velocity in the event that both the radial and azimuthal three standard deviation interval is larger than the high Nyquist velocity. Of the gates that remain, the velocities in the mean difference field near $\delta = \pm(dn_1V_{N1} + dn_2V_{N2})$ are examined further where dn_1, $dn_2 = 0, 1, 2, 3$. We restrict dn_1, $dn_2 = 0, 1, 2, 3$, as most cases will not need higher valued integers, but note that a user could implement additional dn_1, dn_2 values if necessary. We also assume that dn_1, dn_2 are of the same sign. The dn_1, $dn_2 = 0$ case is not necessary to examine. The errors are searched by the general expression: $|\delta - \text{error}| < V_{N1} + V_{N2}$, where dn_1, $dn_2 = 0, \pm 1, \pm 2, \pm 3$ and the error is from Eq. (6). We also note that the error and difference must have the same sign. More specifically, each gate that is $(dn_1V_{N1} + dn_2V_{N2}) - (V_{N1} + V_{N2}) < \delta < (dn_1V_{N1} + dn_2V_{N2}) + (V_{N1} + V_{N2})$ and $\delta > 0$ is corrected by subtracting $(dn_1V_{N1} + dn_2V_{N2})$ from the gate's recorded Doppler velocity value. Similarly, each gate that is $-[(dn_1V_{N1} + dn_2V_{N2}) + (V_{N1} + V_{N2})] < \delta < -[(dn_1V_{N1} + dn_2V_{N2}) - (V_{N1} + V_{N2})]$ and $\delta < 0$ is corrected by adding $dn_1V_{N1} + dn_2V_{N2}$ to the gate's recorded Doppler velocity value. Each possible solution in the correction is retained, resulting in 15 possible solutions. A final (sixteenth) possible solution is the original, recorded Doppler velocity field.

The solutions are compared to an approximate "truth" by evaluating each solution compared to the mean filtered Doppler velocities. As each dn_1, $dn_2 = 0, 1, 2, 3$ solution is

examined, the velocities meeting the search criteria above are flagged as possible errors. Once all possible solutions are computed, the mean filtered field is recomputed with the potential velocity errors removed. Then, the new mean filtered Doppler velocity field is subtracted from each possible solution. For each gate, the solution with the smallest difference compared to its corresponding recomputed mean filtered field value is considered the final solution and the correction (or lack thereof) is retained.

Once all velocities are corrected in the former step, the recorded Doppler velocity is updated. The next step is to follow the same procedure above, but with varying radial and azimuthal filter lengths. Shorter lengths are aimed at correcting randomly distributed processor errors and longer lengths are aimed at correcting grouped and tightly packed random processor errors. The radial (azimuthal) filter is changed to 21, 5, 51, 71, and 5 (9, 5, 21, 71, and 5) gates, respectively. Although additional steps could be implemented or removed via a user-specified option, we found that additional steps did not produce improvements in the hypothetical and real cases to be presented. Alternating filter lengths seems to perform the best in our tests with real cases to target most grouped (longer filter lengths) and random processor errors (shorter filter lengths). After all algorithm steps with each filter length are completed, the Doppler velocity field is considered to have been corrected.

We note that the algorithm is presently implemented in a Python framework and integrates the use of Py-ART (Helmus and Collis 2016), but can easily be manipulated into most programming languages. In our tests, the algorithm is computationally efficient, requiring only ~2–7 s of CPU time for each plan position indicator (PPI). However, an increase in radial and azimuthal resolution of individual PPIs will geometrically increase the time needed for correction per PPI as expected. For the cases examined here, a typical azimuthal (radial) resolution was 0.5–1.0° (75–150 m).

b. Algorithm demonstration

To examine the success of the present algorithm, a simple experiment was designed based on a hypothetical staggered PRT dataset. Using a wind profile reminiscent of the western eyewall of a strong hurricane, a 1.0° PPI was generated with a constant wind field across the PPI (Fig. 3a). The PPI was created by assuming a radar with a 1° beamwidth operating at C band (5 cm wavelength) and a pulse length of 0.5 μs (yielding 75 m range resolution). The "true" Doppler velocities were aliased into two PPIs that correspond with a 4 to 5 PRF ratio for the implementation of the staggered PRT technique. The high PRF was 1400 Hz, the low PRF was 1120 Hz corresponding to the Nyquist velocities of 17.5 and 14.0 m s^{-1}. Noted to be problematic during the application of Eq. (2), the phase noise from the autocorrelation function can cause the estimate of V_C to contain significant error. To replicate such noise, the low and high PRF Doppler velocities were transformed into phase space where noise was added. Random Gaussian noise with a zero mean and a standard deviation of $\pi/12$ radians (corresponding to 1.2 and 1.5 m s^{-1} of Doppler
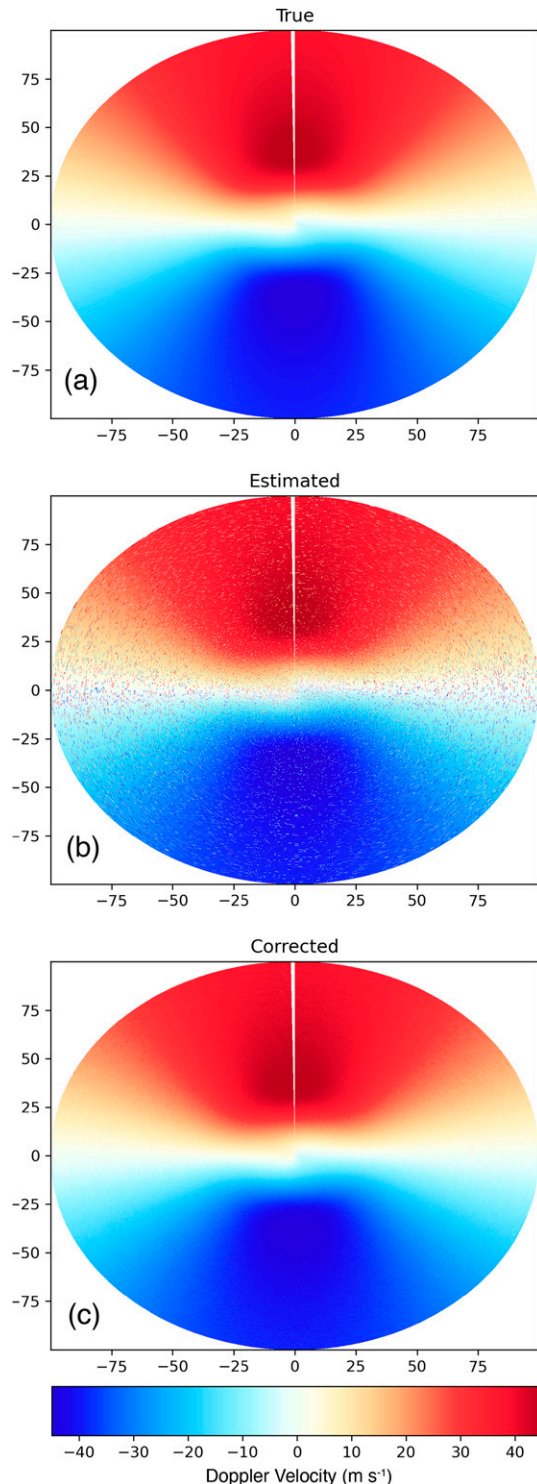
FIG. 3. Doppler velocity correction demonstration using a hypothetical staggered PRT scenario at 1° elevation. (a) The PPI of the true Doppler wind field based on the hypothetical profile is plotted. (b) The Doppler velocities dealiased using the staggered PRT method (with added phase noise). (c) The Doppler velocities from (b) corrected by the algorithm described in section 3a.

velocity noise for the low and high PRF pulses, respectively) was added. Following applications of Eqs. (2)–(6), the Doppler velocities at the high and low PRFs were then dealiased to retrieve the staggered-PRT Doppler velocity estimates (Fig. 3b). To ascertain the total number of errors in the staggered-PRT-derived field, the field was subtracted from the true field. Velocities at adjacent range gates with absolute differences larger than $V_{N1} + V_{N2} = 31.5$ m s^{-1} were assumed to be wrong. In total, more than 29 000 errors were found, suggesting ~6% of velocities were erroneous due to the inaccurate estimation of n via Eq. (3).

The correction procedure summarized in section 3a was applied to the Doppler velocity field in Fig. 3b to retrieve a corrected field. Subtracting the corrected field from the true field and using the error identification criteria shows that the algorithm did not miss any erroneous data according to the error threshold defined above. Similarly, a stricter error threshold of 5 (10) m s^{-1} suggests ~0.5% (0%) of velocities with errors (which accounts for a minimal number of the total velocity points) were missed or misidentified. While the exact number of errors remaining is sensitive to the error threshold chosen, Fig. 3c clearly demonstrates (and simple error computation validates) that very few erroneous velocities remain. We note that similar success was seen for varying degrees of noise added to the phase information and for different PRFs and staggered PRT ratios (e.g., 2:3, 3:4, and 4:5).

4. Applying the staggered PRT algorithm to convective storms

The correction method was developed and tested with three datasets containing low, moderate, and high two-dimensional wind shear. The dimensions are range and azimuth for ground-based radar data (PPI), and rotation angle and range for airborne radar data [range–height indicator (RHI)]. As most data are collected in the PPI mode, application of the staggered PRT processor error correction algorithm to PPI data are presented here, but should yield similar success for RHIs.

The low radial shear regimes are represented by the inner core region of Hurricane Isaac (2012) and the trailing stratiform region of an MCS. The Hurricane Isaac data were collected by the dual polarimetric C-band SMART radar on 29 August 2012 while the MCS data were collected by the X-band DOW6 radar on 26 June 2015 in northern Kansas. While the vertical shear of the horizontal wind is high in a hurricane, the gate-to-gate shear within a single PPI is relatively low. Moderate range-and-azimuth shear is represented by the transition region of the MCS sampled by DOW6. The convective region of the MCS provided a high shear regime within which to evaluate the correction algorithm. Additionally, a tornadic supercell, observed by the dual polarimetric SMART radar on 5 June 2009 during VORTEX2 (Wurman et al. 2012) was also used to examine the correction algorithm performance for high shear data. Details of each radar dataset are listed in Table 1.

a. MCS case

The 26 June 2015 MCS formed to the northwest of DOW6's location and propagated southeast (Miller et al. 2020). The

TABLE 1. Summary and attributes of radar data employed to test the staggered PRT/dual PRF dealiasing algorithm in the current study. The acronym "TDR" stands for the "tail Doppler radar" on the NOAA P-3. The Shared Mobile Atmospheric Research and Teaching (SMART) Radar 2 is denoted "SR2."

Case	Radar	Extended Nyquist mode	Extended Nyquist (m s^{-1})	PRF ratio	V_{N1}, V_{N2} (m s^{-1})
PECAN MCS	DOW6	Staggered PRT	33.5 or 59.7	5:4	6.7, 8.4 or 11.9, 14.9
Hurricane Isaac	SR2	Staggered PRT	48.0	3:2	16.0, 24.0
VORTEX2 supercell	SR2	Staggered PRT	40.2	3:2	13.3, 20.0
VORTEX-SE supercell	TDR	Dual PRF	50.0	3:2	16.7, 25.0

initially isolated convective cells merged into a convective line, producing a leading-line trailing-stratiform MCS (e.g., Biggerstaff and Houze 1991). Due to the inhomogeneity of the individual updrafts, radial and azimuthal shear was high between the individual cells. In addition, the 5:4 staggered

PRT ratio used by DOW6 increased the rate of observed processor errors (e.g., Joe and May 2003). Staggered PRT processor errors were particularly extensive in regions of the strongest shear (cf. the area enclosed by the dashed red contour in Fig. 4c). Despite the high error rate, the correction algorithm
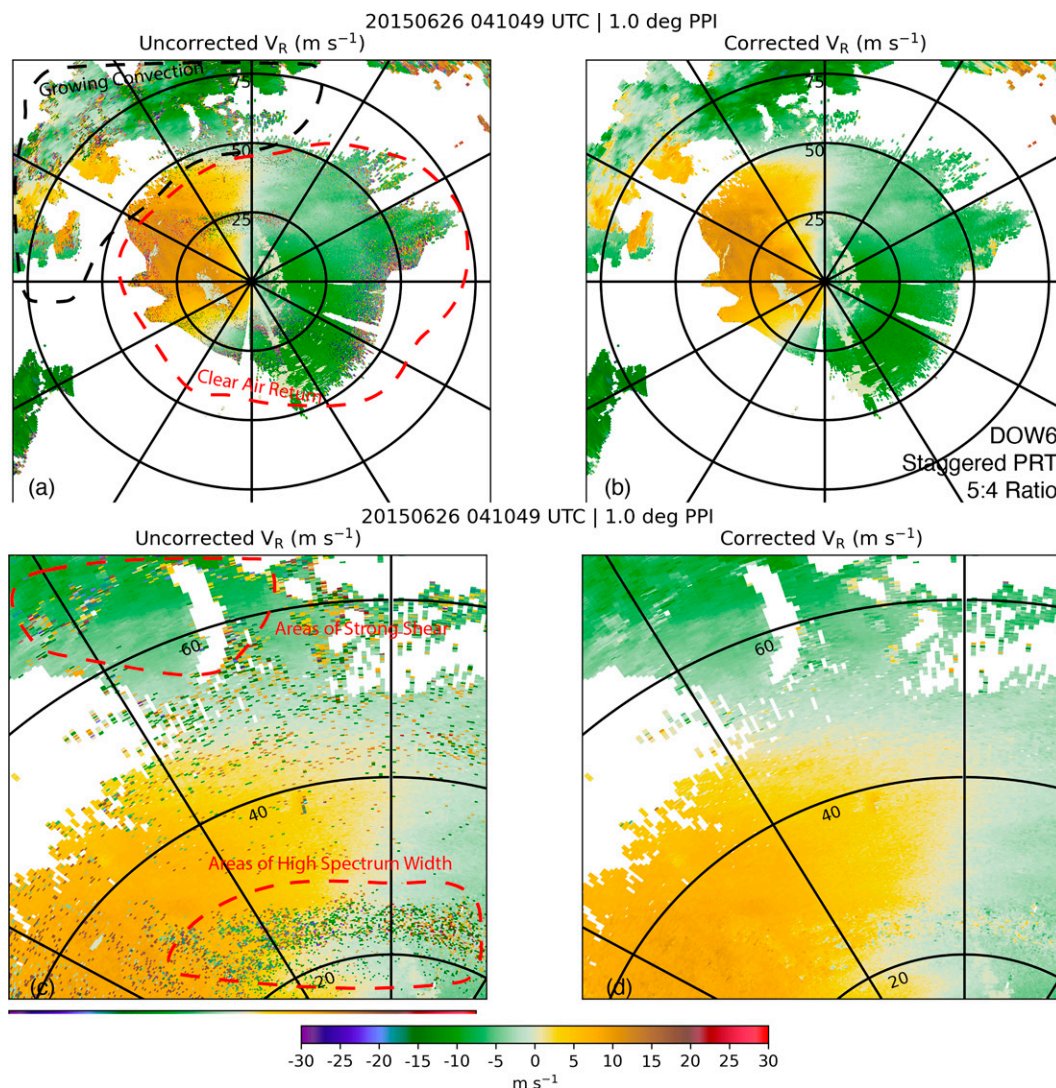

FIG. 4. Radial velocity observations at 1.0° elevation for the MCS observed at 0410:49 UTC 26 Jun 2015 from DOW6 during PECAN. Shown are the (a) uncorrected velocity, (b) corrected velocity, (c) magnified view of the uncorrected velocities, and (d) magnified view of the corrected velocities. All velocities are in m s^{-1} according to the color scale.
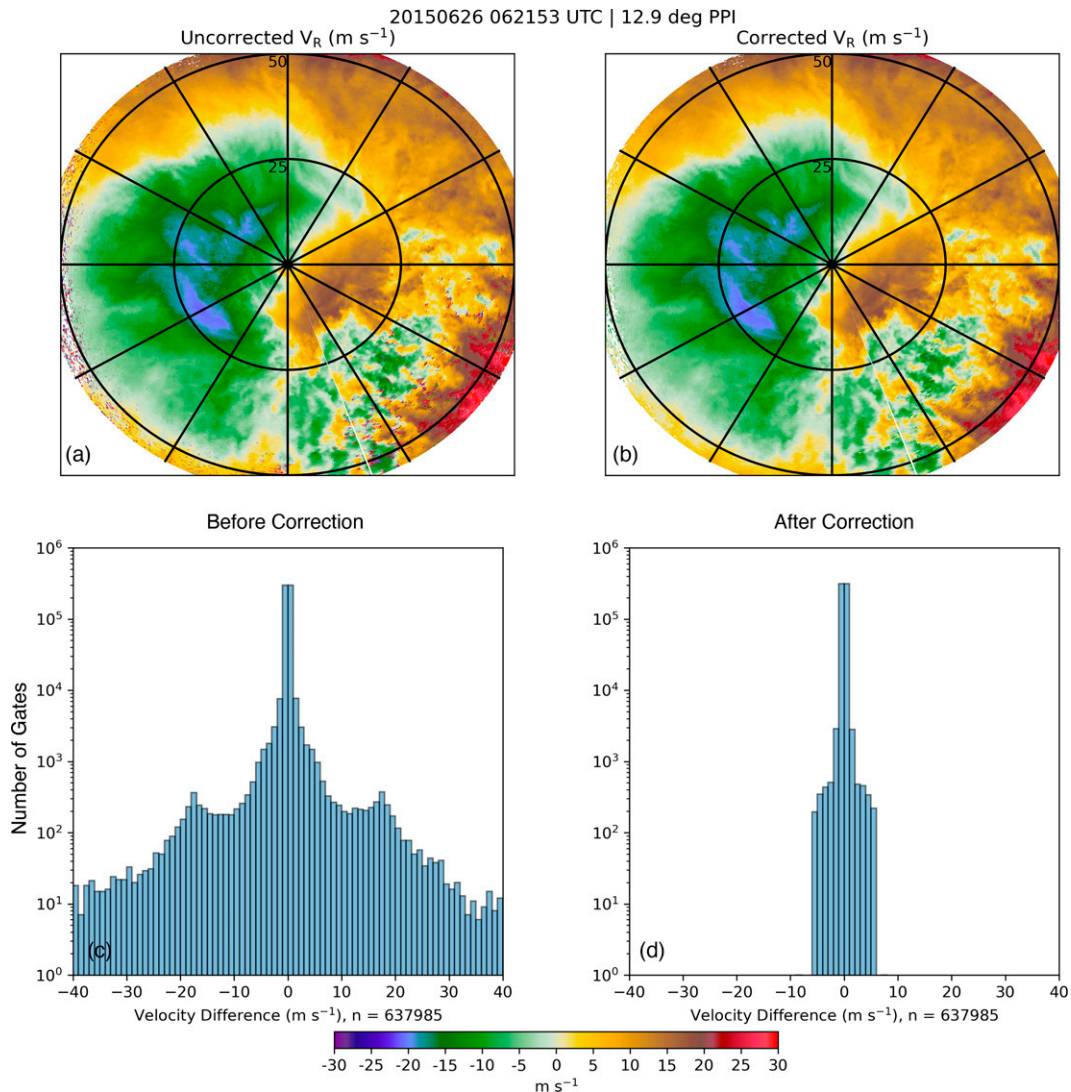
FIG. 5. (a) Uncorrected and (b) corrected radial velocity, in m s^{-1} according to the color scale, for the 12.9° elevation angle PPI taken at 0621:53 UTC 26 Jun 2015 by DOW6 during PECAN. The difference distribution distribution relative to the mean smoothed radial velocity field (c) before and (d) after the correction algorithm was applied. The number of gates (n) is shown in the x-axis label.

developed here was successful in dealiasing the speckled velocities, even in the lower signal-to-noise clear-air region associated with biological scatterers within the first 40 km range from DOW6 (Fig. 4). Moreover, the points near the edges of echoes and points within the maximum of shear with large gradients of radial and azimuthal velocity were properly identified and corrected. Due to the high error rate and subsequent clustering of errors between convective cells, this case in particular demonstrates the utility of the one-dimensional method over a two-dimensional method (Fig. 2). In particular, the earlier two-dimensional methods illustrated in Fig. 2 result in remaining clusters of errors where those algorithms are unable to operate correctly in regions of high density speckled erroneous velocities. The progression of such algorithms generally results in a "consolidation" of the errors into a blocklike error cluster, which

is generally not improved by additional iterations of those filters. Here, the SGF-based technique is clearly superior and leaves significantly less groups of errors after the algorithm completion.

The performance of the present correction procedure in the 26 June 2015 MCS is further illustrated using data from the convective region at higher elevation angles (Fig. 5). Once again, significant processor errors occur in the high shear regions associated with gradients around the edges of the convective cores, especially when the sign of the velocity changes. A histogram of the mean difference field before correction (Fig. 5c) demonstrates that velocities that require correction are clearly different from the surrounding local flow. As previously described, the algorithm assumes that the SGF flow is more representative of the magnitude of the true flow. Differences near 0 m s^{-1}, which dominate the histogram, are
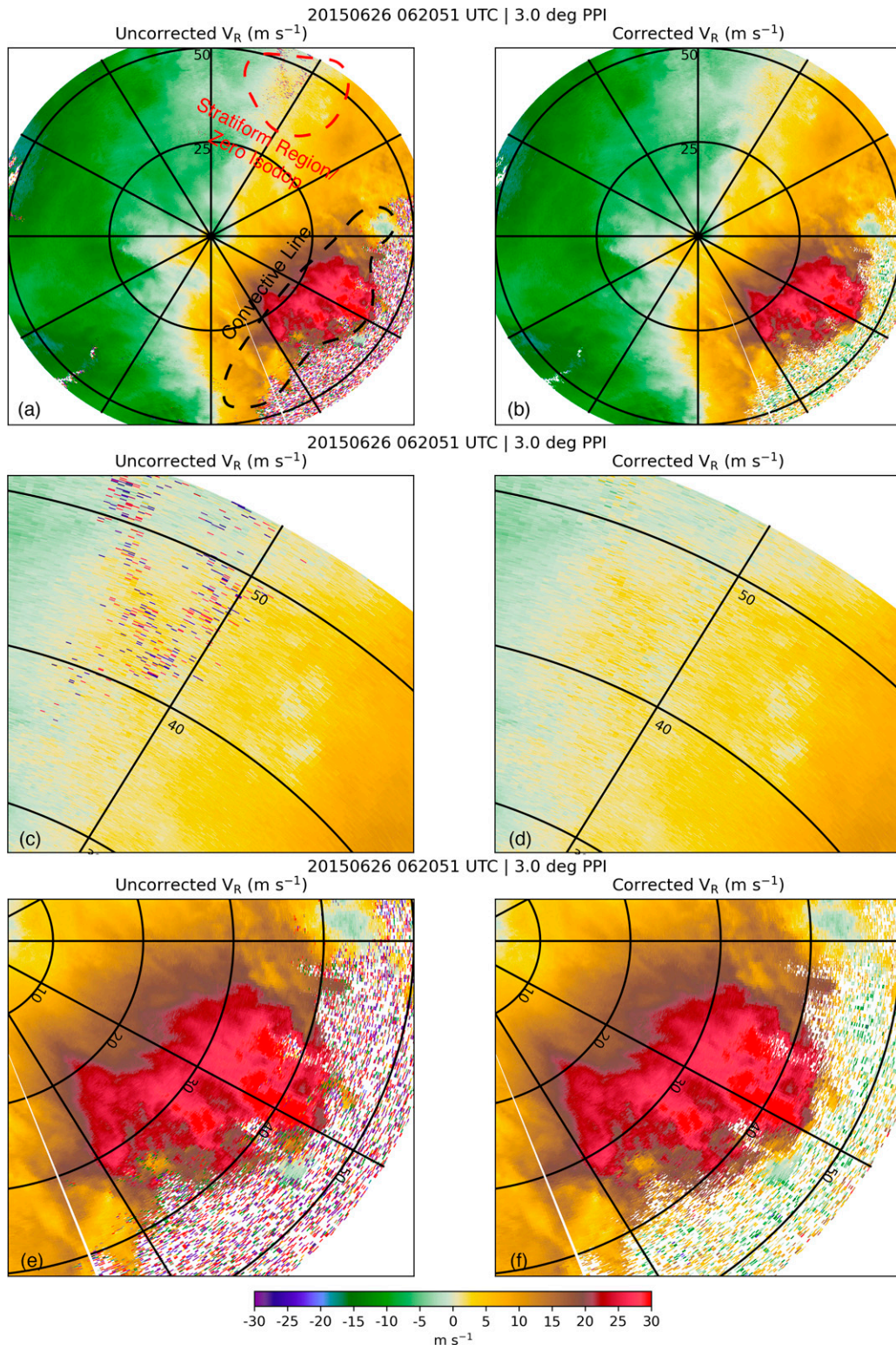
FIG. 6. (a) Partially quality-controlled, and uncorrected radial velocity at 3.0° elevation from DOW6 at 0620:51 UTC 26 Jun 2015, (b) corrected radial velocities, (c) magnified view of uncorrected velocities from the stratiform region highlighted by the dashed red curve in (a), (d) corrected velocities from (c), (e) magnified view of uncorrected velocities from convective region highlighted by the dashed black contour in (a), and (f) corrected velocities from (d). All velocities are in m s^{-1} according to the color scale.
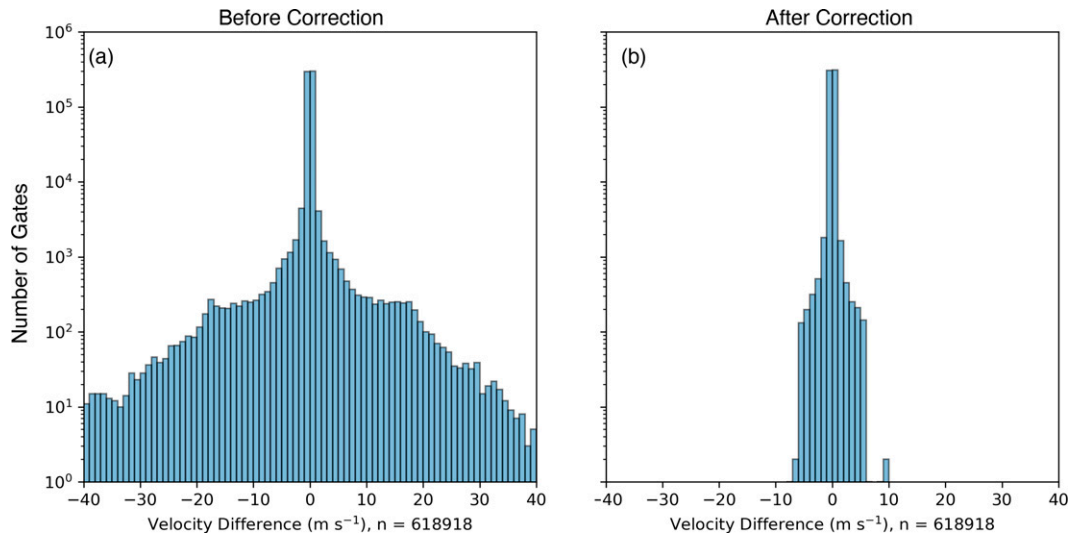
FIG. 7. Histogram of the mean difference field corresponding to velocities shown in Fig. 6. (a) The normal distribution of the difference field prior to any corrections. (b) The final normal distribution of the difference field after all corrections were applied.

assumed to be correct. After the correction algorithm has been applied (Fig. 5b), the data appear to be much less noisy and the standard deviation of the difference distribution is significantly reduced (Fig. 5d). Gates with velocity differences greater (less) than 10 (-10) m s^{-1} are few, suggesting the algorithm is successful in correcting erroneous velocities to be consistent with the local flow.

As the MCS continued to propagate southeast, DOW6 sampled more of the trailing stratiform region (Fig. 6). Although the stratiform region was largely free of staggered PRT processor errors, additional processor errors were apparent in regions of moderate shear close to the MCS's transition zone (e.g., Biggerstaff and Houze 1991). For example, Fig. 6a shows the 3.0° elevation angle staggered PRT radial velocity observations from DOW6 at 0620:51 UTC. The observations are shown after some basic quality control steps were taken using the Py-ART software suite (Helmus and Collis 2016); e.g., low reflectivity < -10 dBZ had been removed, but prior to staggered PRT processor error corrections. It should be noted that no velocity dealiasing was required, as the extended maximum unambiguous velocity for this particular volume was 59.7 m s^{-1} relative to much weaker deep-tropospheric shear. However, typical velocity dealiasing (e.g., the region-based method in Py-ART) should be executed first prior to applying the algorithm described here. Figure 6b shows the radial velocity field after the staggered PRT processor errors were identified and corrected. Gates within the stratiform region near the zero isodop (Figs. 6a,c,d) also show similar results with nearly all erroneous speckled velocities corrected. These regions are nearer the deep convection where shear and spectrum width are expected to be stronger and processor errors more numerous. Of particular interest, the convective region center (i.e., as indicated in Fig. 6a) is characterized by multiple velocities which are significantly higher or lower than their surrounding gates (Figs. 6e,f). After applying

the correction algorithm, the region is free of speckled processor error points and all velocities were corrected.

The impact of the correction algorithm on the MCS data is further elucidated by examining distributions of the difference fields before and after the correction algorithm has been applied (Fig. 7). Using the data from Fig. 6, the histogram of the mean difference field is shown before (Fig. 7a) and after (Fig. 7b) correction. All velocities with absolute difference values greater than 10 m s^{-1} were identified and corrected. In total, $>11\,000$ corrections were made, many of which likely were in the noise beyond the convective line. We retain the noise here to demonstrate that the coherent velocities (e.g., within the convective line; Figs. 6e,f) will be used to correct speckled, incoherent velocities left in PPIs. However, the correction of the data within the convective line seems unaffected by the nearby incoherent noise, showing the utility of the SGF in identifying the true local flow. We also use this illustrative example to emphasize that the present algorithm should be applied following other quality control procedures.

b. Hurricane Isaac

Similar to the stratiform region of the MCS observed by DOW6 during PECAN, minimal dealiasing was required for the inner core region of Hurricane Isaac sampled by the SMART radar (Fig. 8). The primary area where the processor errors occurred was within the inbound velocity region centered around 35 m s^{-1} (Fig. 8a). Numerous velocities in excess of -50 m s^{-1} were embedded in the inbound flow. The algorithm correctly identified and dealiased those points. In tests of median-filter-based methods previously discussed in sections 1 and 2, this particular PPI was left with several blocklike groups of processor errors (not shown here, but similar to errors remaining in Fig. 2). The median-filter-based techniques can seemingly consolidate dense speckles
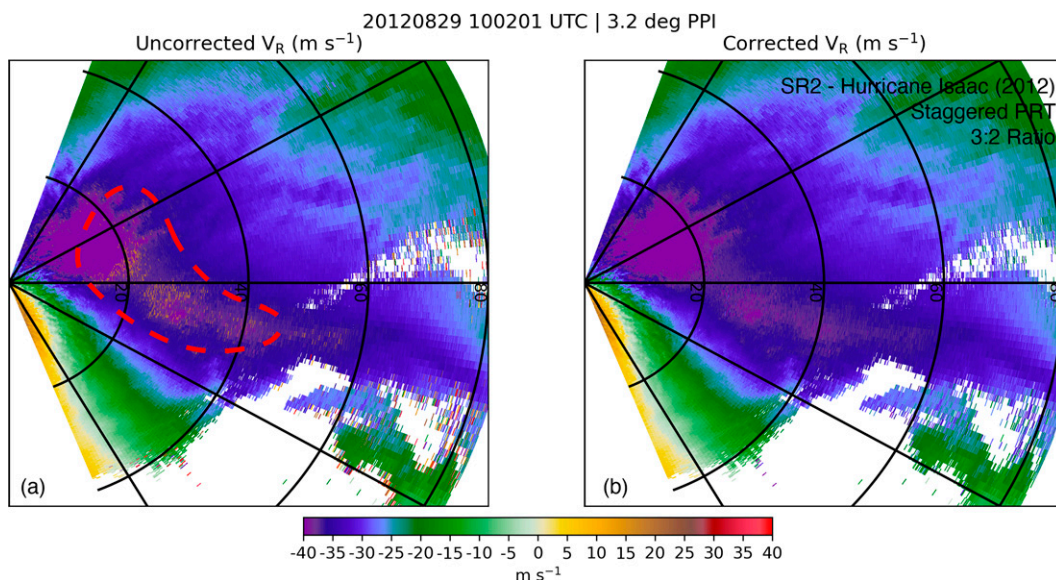
FIG. 8. (a) Uncorrected and (b) corrected radial velocity at 3.2° elevation angle, in m s^{-1} according to the color scale, from SR2 observed at 1002:01 UTC 29 Aug 2012 during Hurricane Isaac. The dashed red curve in (a) highlights a region of particularly dense processor errors that typically result in remaining errors in median-filter-based identification methods.

into a single, unified group of erroneous velocities. Here, using the SGF-based technique, these dense speckles are easily identified and corrected leaving no remaining errors. An earlier version of the SGF-based algorithm was applied to a landfalling hurricane (Hurricane Irene, 2012) in Alford et al. (2020), which showed similar success to the case seen here.

c. Goshen County tornadic supercell

During observation of the Goshen County, Wyoming, supercell that occurred during VORTEX 2 on 5 June 2009, SMART radar 2 was using a staggered PRT ratio of 3:2, which limited the number of processor errors. Nevertheless, numerous erroneous velocities were found both near the low-level mesocyclone and aloft in regions of strong radial shear. The correction of errors near the mesocyclone is of particular importance for diagnosing sub-mesocyclone-scale circulations in supercells (e.g., May 2001; Skinner et al. 2014; DiGangi et al. 2016; Betten et al. 2018).

Figure 9a shows the uncorrected radial velocity field that had undergone similar preliminary quality control as conducted for the MCS case above. Processor errors were largely confined to the mesocyclone region near $x = -5$ km, $y = 15$ km, but some errors existed in the forward flank near the boundaries of the radial velocity data. After the correction algorithm was applied, all visible erroneous velocities in the forward flank were corrected successfully except for a few residual velocity errors on the edge of the coherent echo. Despite the numerous processor mistakes near the mesocyclone (Fig. 9c), the correction algorithm successfully dealiased the data and preserved the mesocyclone structure, especially in the center of the mesocyclone where gate-to-gate shear approached 60 m s^{-1}. The character of the surrounding flow was also preserved in, for example, the regions of radial convergence on the north side of the

mesocyclone denoted by the dashed black lines in Fig. 9c. The processor errors, when corrected, yielded a velocity field that smoothly transitioned azimuthally and radially across the flow regimes (Fig. 9d). In the past, the processor errors would have been deleted, rather than corrected, leading to improperly diagnosing the magnitude and scale of the convergence pattern. Examination of subsequent sweeps where gate-to-gate shear was strong in the low levels (not shown) suggests that the algorithm routinely preserved the correct radial velocity structure.

d. Errors in the correction

In median-filter-based correction algorithms, a radially and azimuthally extensive region with similar processor errors can be interpreted by the algorithm as the background flow as previously noted. In such cases, the sparse velocities within the region or velocities near the region representing the actual background flow will be incorrectly assigned an aliased velocity (Altube et al. 2017). As highlighted by several PPIs here (e.g., Fig. 2 versus Figs. 4 and 8), the SGF-based algorithm significantly improves error identification in regions of densely grouped errors.

We briefly turn to regions of strong radial shear in the Goshen County case that could potentially exemplify the largest (albeit limited) source of uncertainty in the algorithm's success. As in the low levels (Fig. 9), the upper levels (Fig. 10) of the supercell case originally contained processor errors possessing both radial and azimuthal continuity. Applying the algorithm yielded several instances of velocities that were seemingly missed (e.g., Fig. 10b). Erroneous velocities in Fig. 10d were corrected into an interval that appears consistent with the surrounding background magnitude, although the resulting flow structure was visually somewhat complex. It should be noted that such locally large azimuthal shear after
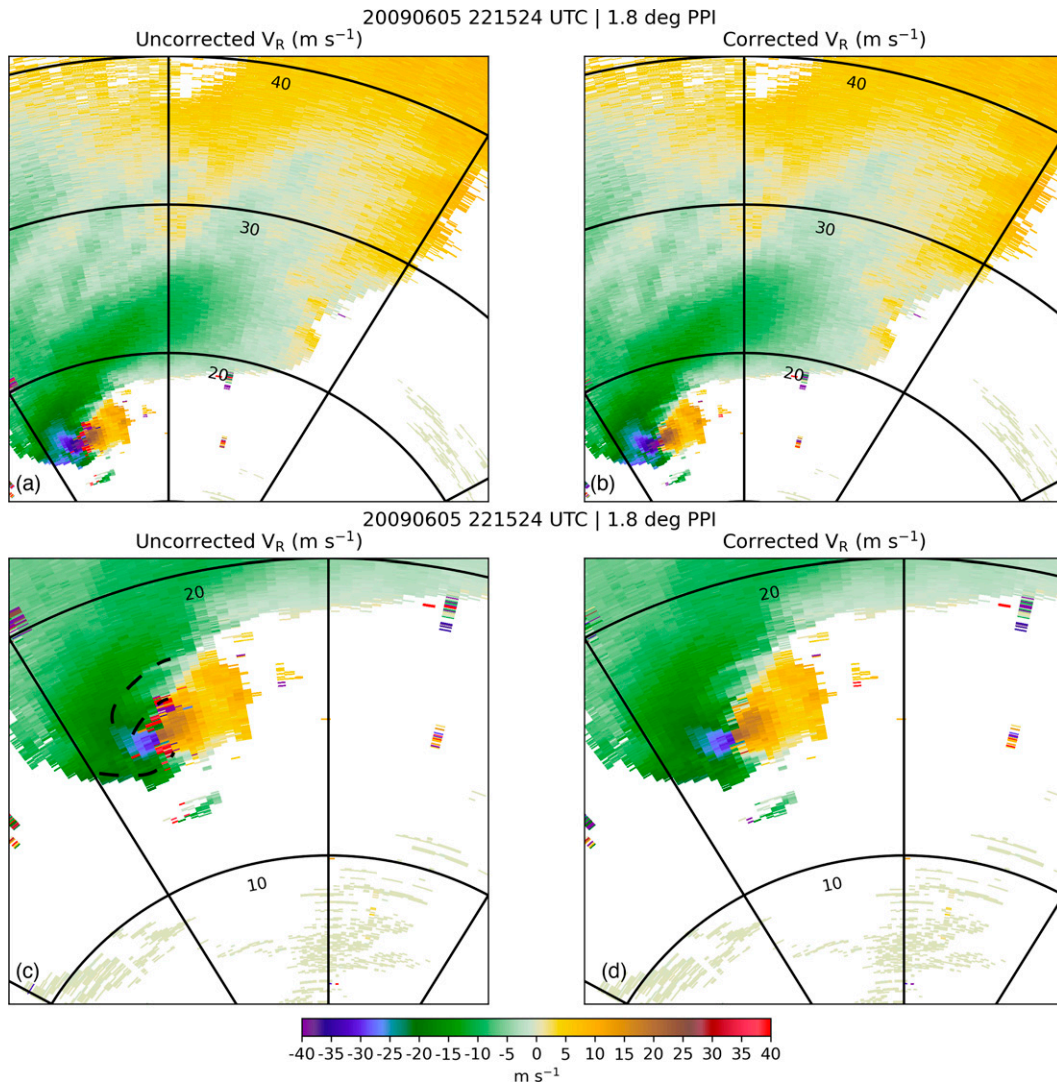
20090605 221524 UTC | 1.8 deg PPI

20090605 221524 UTC | 1.8 deg PPI

FIG. 9. (a) Uncorrected and (b) corrected radial velocity at 1.8° elevation angle, in m s^{-1} according to the color scale, from SR2 observed at 2215:24 UTC 5 Jun 2009 for a tornadic supercell observing during VORTEX2. The mesocyclone area in (a) is magnified for (c) uncorrected and (d) corrected radial velocities. The dashed curves in (c) annotate regions of radial divergence.

velocity correction, which are not unique to this SGF-based correction method and represent similar uncertainty in other techniques, could conceivably arise from actual large shears that are at the effective resolution limit of a given radar system. In general, however, the staggered PRT correction method clearly offered significant improvement over either the strict deletion of processor errors or else improper attempts to dealias the points by adding intervals of just the low or just the high Nyquist velocities as is done in previous correction techniques.

5. Application to dual PRF processing

Existing dual PRF processor error correction algorithms use a single-pass or double-pass two-dimensional window to identify aliased points. For the case of staggered PRT data as

previously examined in section 4, it was determined that the iterative SGF-based method performed better, especially in the presence of numerous and extensively grouped errors. In this section, the same identification procedures are applied to dual PRF processor errors to determine if the SGF-based procedure also performs well for the latter types of datasets.

While the identification portion of the algorithm is the same, the correction step has been modified to account for the different characteristics of the dual PRF processor velocity errors. In contrast to the staggered PRT algorithm in which the errors are near $\pm(dn_1 V_{N1} + dn_2 V_{N2})$, the expected errors for dual PRF signal processing are near $\pm 2n V_{N2}$ and $\pm 2n V_{N1}$ (where $n = 1, 2, 3, \dots$). Thus, the correction portion of the algorithm has been modified to partition the mean difference field into regions near $\pm 2n V_{N2}$ and $\pm 2n V_{N1}$ with
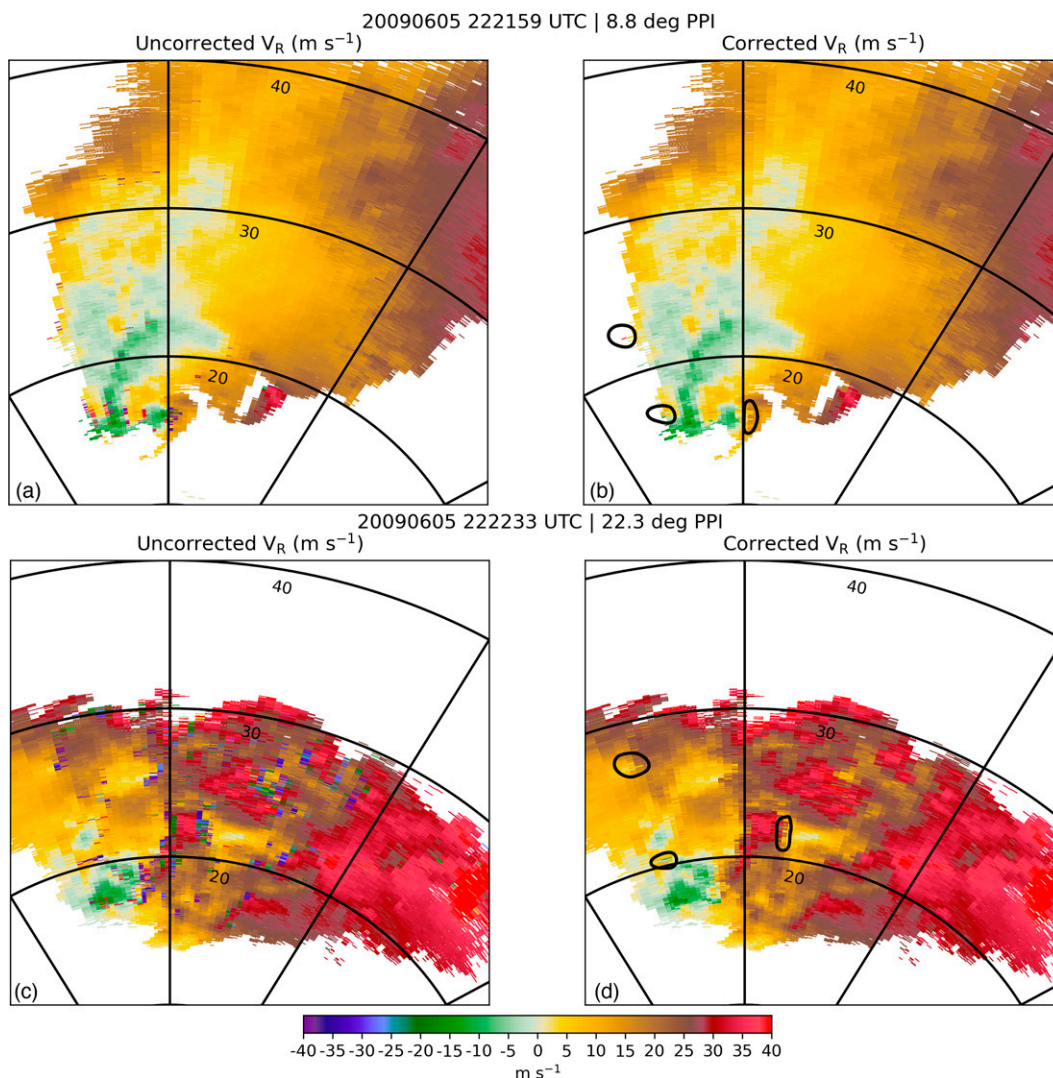
FIG. 10. (a) Uncorrected and (b) corrected radial velocity at the 8.8° elevation angle for the tornadic supercell sampled by SR2 at 2221:59 UTC 5 Jun 2009. (c) Uncorrected and (d) corrected radial velocity at the 22.3° elevation angle for the tornadic supercell sampled by SR2 at 2222:33 UTC 5 Jun 2009. All velocities are in m s^{-1}, according to the color scale. The black contours highlight regions of missed or uncertain corrections made.

interval widths of $\pm 2n V_{N2}$ and $\pm 2n V_{N1}$. When the Nyquist velocity of the individual ray is unknown, a comparison of individual points to their surrounding neighbors is sufficient to determine the proper magnitude of the required correction.

The dual PRF version of the algorithm has already been tested across several different radar platforms for a variety of cases. Here, dual PRF observations from one of the dual X-band, tail Doppler radars (TDRs) on board the NOAA P-3 aircraft (e.g., Jorgensen et al. 1983; Ziegler et al. 2001) obtained in a supercell storm on 5 April 2017 (Jorgensen et al. 2017) during the VORTEX-SE project (NSSL 2018) are used to illustrate the utility of the SGF-based identification method in a second high shear data case. The uncorrected data (Fig. 11a) have numerous processor errors, as well as several missing data points which challenges the data continuity

requirement of the correction algorithm. The unusually large number of missing data points in this case, which resulted from a large signal quality index (SQI) threshold value having been applied on this particular mission to the raw data stream recording, present an additional opportunity to demonstrate the robustness of the current processor error correction algorithm. Note that SQI, a quantity often utilized by Vaisala radar signal processors, is related to the spectrum width, and gates with low SQI imply that the spectrum width is large. Where SQI is large, the spectrum width is typically narrower and if utilized as a quality control tool, can reduce the rate of the dual PRF (or staggered PRT) processing errors. Nevertheless, dual PRF (and staggered PRT) errors often remain even for thresholds of relatively high SQI. In this case, the TDR's ~2° beamwidth, combined with its large (120° s^{-1})
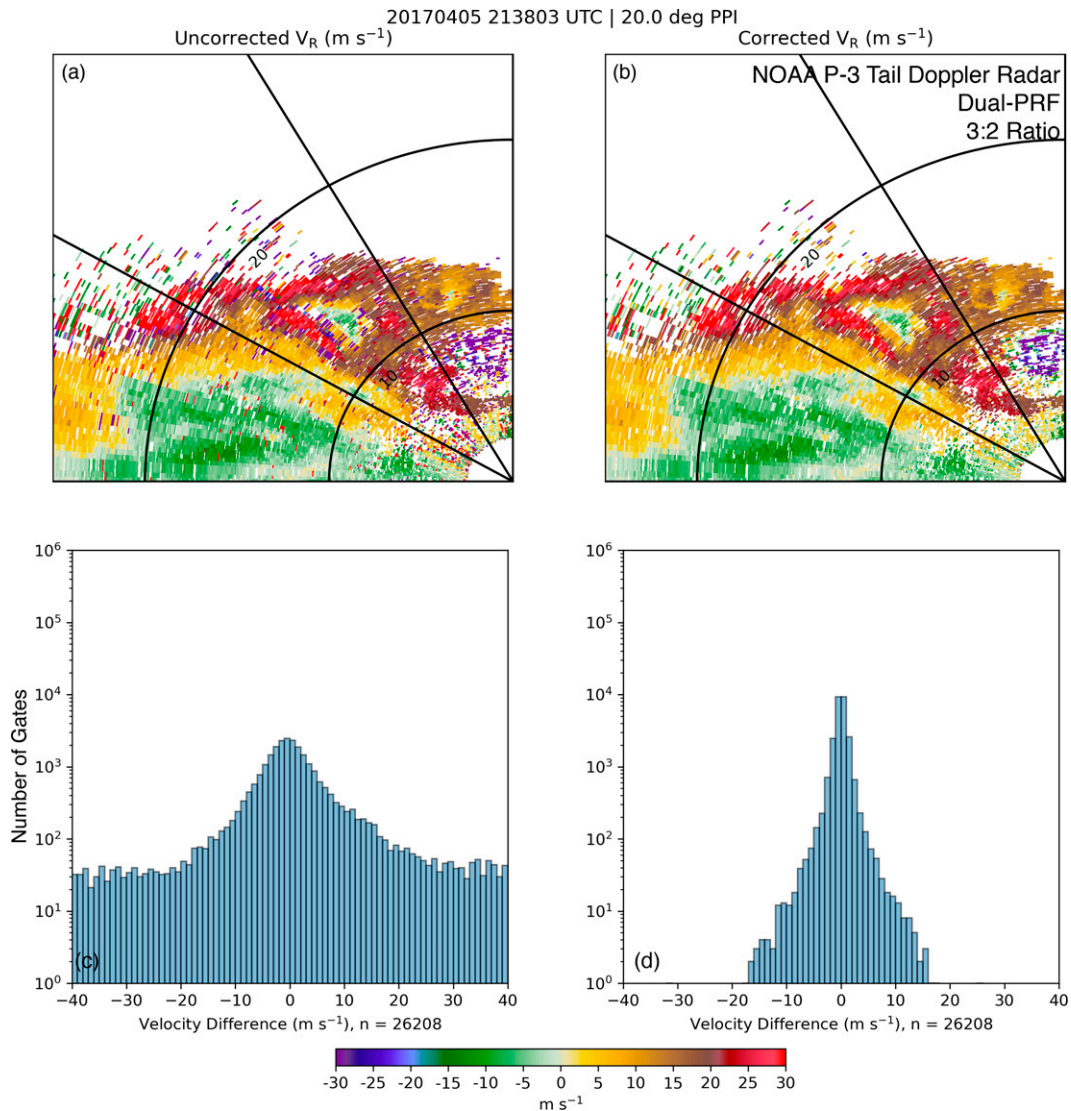
FIG. 11. (a) Uncorrected radial velocity from the 20° forward scan from the NOAA P-3 tail Doppler radar. (b) Corrected radial velocity after the application of the dual PRF version of the correction algorithm. The difference distribution relative to the mean smoothed radial velocity field (c) before and (d) after the correction algorithm was applied.

antenna rotation rate, results in significant spectrum width broadening in regions of high vertical wind shear (Doviak and Zrnić 2006) that commonly occur in TDR observations of supercell storms (e.g., Ziegler et al. 2001) and hurricanes. Since the SQI threshold is applied before recording, these missing data unfortunately cannot be retrieved.

Despite the significant number of processor errors and the high frequency of missing data points, the correction algorithm performed well (Fig. 11b). Visually, it appears that all processor errors were properly identified by the SGF-based procedure and corrected using the modified partitions in the dealiasing step. To quantify the performance, the mean difference field histograms before and after correction are shown in Figs. 11c and 11d. After the algorithm was applied, nearly all

points beyond ± 15 m s^{-1} were corrected, significantly reducing the range of the distribution. The behavior of the modified staggered PRT identification for dual PRF processor errors appears to have similar success to the staggered PRT correction method.

6. Summary and conclusions

The characteristics of the Zrnić and Mahapatra (1985) staggered PRT signal velocity processing errors have been documented and used to develop a velocity correction algorithm that was tested using mobile radar data collected during a mature midlatitude MCS, the inner core of a landfalling hurricane, and a tornadic supercell. The identification procedure within

the algorithm is based on combining radial and azimuthal SGF Doppler velocities with varying window lengths that vary systematically to capture and correct speckled and small clusters of processor errors. The recorded Doppler velocities are then compared to the recomputed filtered field to identify staggered PRT velocity errors. For the data examined here, this identification procedure was superior to single-pass or multipass two-dimensional median-filter-based algorithms used in existing dual PRF correction procedures. In particular, the identification of grouped velocity errors was more readily corrected with the use of the SGF-based identification.

Application of the new identification procedure to dual PRF velocity data from one of the dual tail Doppler radars aboard the NOAA P-3 obtained from a supercell showed that the algorithm described here performed equally well for both dual PRF and staggered PRT datasets. Hence by modifying the dealiasing portion of the algorithm to account for the differences in velocity error characteristics for dual PRF versus staggered PRT signal processing, a single unified, robust algorithm has been created to correct velocity data from both staggered PRT and dual PRF signal processing methods.

It is important to note that the algorithm requires some minimal degree of spatial data continuity to determine an appropriate background flow. Hence, isolated velocity points that are originally aliased may not be corrected. For cases in which the original processor velocity errors are clustered in both radial and azimuthal directions, with similar aliased velocities that cover a contiguous area greater than the size of the identification windows, the algorithm may identify the aliased velocity as the correct background flow. Subsequent velocity corrections may improperly dealias correct velocities within and near the cluster into the aliased velocity interval. Similar scenarios have been reported for the existing dual PRF correction algorithms, particular for clusters of processor velocity errors on the scale of the one- or two-dimensional windows. However, no such cases were found with the datasets presented here since most clustered errors were easily identified by the algorithm, particularly those on the scale of previous identification windows (e.g., 3×3 two-dimensional window).

Even though the staggered PRT velocity data for the convective region of the MCS examined here appear to have a greater number of problematic errors clusters than the dual PRF datasets used in previous studies (e.g., Joe and May 2003), there were relatively few instances of improperly dealiased velocities or missed velocity errors after applying the correction algorithm based on our inspection. Moreover, as shown by the distribution of differences from the window median velocity before and after the correction, the algorithm significantly reduced the width of the velocity difference field distribution for each dataset examined. The algorithm documented here has already been successfully employed by the coauthors as well as investigators at other institutions for a number of cases across several radar platforms and weather scenarios. Of particular importance for high shear convective storms, the correction algorithm was shown to properly dealias velocities and retain the structure of convergent rotational flow within a tornadic mesocyclone, in addition to performing

well for the landfalling hurricane and midlatitude MCS cases. Considering that, in the past, staggered PRT processor velocity errors often had to be deleted from datasets using tedious manual editing methods, the algorithm developed here holds the promise of greatly assisting increased research productivity. In the future, it may be useful to integrate this algorithm (or aspects of) with existing dealiasing algorithms such as the immensely successful two-dimensional velocity dealiasing algorithm used by the WSR-88Ds and applied to research and/or operational datasets.

Data availability statement. The data associated with this research, along with a Python-based version of software containing the algorithm, are available at https://github.com/aaddisonalford/processorCorrect.

REFERENCES

Alford, A. A., M. I. Biggerstaff, G. D. Carrie, J. L. Schroeder, B. D. Hirth, and S. M. Waugh, 2019a: Near-surface maximum winds during the landfall of Hurricane Harvey. *Geophys. Res. Lett.*, **46**, 973–982, https://doi.org/10.1029/2018GL080013.

——, ——, and ——, 2019b: Mobile ground-based SMART radar observations of Hurricane Harvey (2017). *Geosci. Data J.*, **6**, 205–213, https://doi.org/10.1002/gdj3.82.

——, J. A. Zhang, M. I. Biggerstaff, F. D. Marks, P. Dodge, and D. J. Bodine, 2020: Transition of the hurricane boundary layer during the landfall of Hurricane Irene (2011). *J. Atmos. Sci.*, **77**, 3509–3531, https://doi.org/10.1175/JAS-D-19-0290.1.

Altube, P., J. Bech, O. Argemi, T. Rigo, N. Pineda, S. Collis, and J. Helmus, 2017: Correction of dual-PRF Doppler velocity outliers in the presence of aliasing. *J. Atmos. Oceanic Technol.*, **34**, 1529–1543, https://doi.org/10.1175/JTECH-D-16-0065.1.

Atlas, D., and Coauthors, 1963: *Severe Local Storms. Meteor. Monogr.*, No. 5, Amer. Meteor. Soc., 242 pp.

Betten, D. P., M. I. Biggerstaff, and C. L. Ziegler, 2018: Three-dimensional storm structure and low-level boundaries at different stages of cyclic mesocyclone evolution in a high-precipitation tornadic supercell. *Adv. Meteor.*, **2018**, 9432670, https://doi.org/10.1155/2018/9432670.

Biggerstaff, M. I., and R. A. Houze Jr., 1991: Midlevel vorticity structure of the 10–11 June 1985 squall line. *Mon. Wea. Rev.*, **119**, 3066–3079, https://doi.org/10.1175/1520-0493(1991)119<3066:MVSOTJ>2.0.CO;2.

——, and Coauthors, 2005: The Shared Mobile Atmospheric Research and Teaching radar: A collaboration to enhance research and teaching. *Bull. Amer. Meteor. Soc.*, **86**, 1263–1274, https://doi.org/10.1175/BAMS-86-9-1263.

Crum, T. D., and R. L. Alberty, 1993: The WSR-88D and the WSR-88D Operational Support Facility. *Bull. Amer. Meteor. Soc.*, **74**, 1669–1687, https://doi.org/10.1175/1520-0477(1993)074<1669:TWATWO>2.0.CO;2.

Dazhang, T., S. G. Geotis, R. E. Passarelli Jr., A. L. Hansen, and C. L. Frush, 1984: Evaluation of an alternating-PRF method for extending the range of unambiguous Doppler velocity. *22nd Conf. on Radar Meteorology*, Zurich, Switzerland, Amer. Meteor. Soc., 523–527.

DiGangi, E. A., D. R. MacGorman, C. L. Ziegler, D. Betten, M. Biggerstaff, M. Bowlan, and C. K. Potvin, 2016: An overview of the 29 May 2012 Kingfisher supercell during DC3. *J. Geophys. Res. Atmos.*, **121**, 14 316–14 343, https://doi.org/10.1002/2016JD025690.

Dong, J., and M. Xue, 2013: Assimilation of radial velocity and reflectivity data from coastal WSR-88D radars using an ensemble Kalman filter for the analysis and forecast of landfalling Hurricane Ike (2008). *Quart. J. Roy. Meteor. Soc.*, **139**, 467–487, https://doi.org/10.1002/qj.1970.

Doviak, R. J., and D. S. Zrnić, 2006: *Doppler Radar and Weather Observations.* 2nd ed. Dover Publications, 592 pp.

——, V. Bringi, A. Ryzhkov, A. Zahrai, and D. Zrnić, 2000: Considerations for polarimetric upgrades to operational WSR-88D radars. *J. Atmos. Oceanic Technol.*, **17**, 257–278, https://doi.org/10.1175/1520-0426(2000)017<0257:CFPUTO>2.0.CO;2.

Helmus, J. J., and S. M. Collis, 2016: The Python ARM Radar Toolkit (Py-ART), a library for working with weather radar data in the Python programming language. *J. Open Res. Software*, **4**, e25, https://doi.org/10.5334/jors.119.

Holleman, I., and J. Beekhuis, 2003: Analysis and correction of dual-PRF velocity data. *J. Atmos. Oceanic Technol.*, **20**, 443–453, https://doi.org/10.1175/1520-0426(2003)20<443:AACODP>2.0.CO;2.

James, C. N., and R. A. Houze Jr., 2001: A real-time four-dimensional Doppler dealiasing scheme. *J. Atmos. Oceanic Technol.*, **18**, 1674–1683, https://doi.org/10.1175/1520-0426(2001)018<1674:ARTFDD>2.0.CO;2.

Joe, P., and P. T. May, 2003: Correction of dual PRF velocity errors for operational Doppler weather radars. *J. Atmos. Oceanic Technol.*, **20**, 429–442, https://doi.org/10.1175/1520-0426(2003)20<429:CODPVE>2.0.CO;2.

——, D. Burgess, R. Potts, T. Keenan, G. Stumpf, and A. Treolar, 2004: The S2K severe weather detection algorithms and their performance. *Wea. Forecasting*, **19**, 43–63, https://doi.org/10.1175/1520-0434(2004)019<0043:TSSWDA>2.0.CO;2.

Jorgensen, D. P., P. H. Hildebrand, and C. L. Frush, 1983: Feasibility test of an airborne pulse-Doppler meteorological radar. *J. Climate Appl. Meteor.*, **22**, 744–757, https://doi.org/10.1175/1520-0450(1983)022<0744:FTOAAP>2.0.CO;2.

——, T. R. Shepherd, and A. S. Goldstein, 2000: A dual-pulse repetition frequency scheme for mitigating velocity ambiguities of the NOAA P-3 airborne Doppler radar. *J. Atmos. Oceanic Technol.*, **17**, 585–594, https://doi.org/10.1175/1520-0426(2000)017<0585:ADPRFS>2.0.CO;2.

——, C. L. Ziegler, E. N. Rasmussen, A. S. Goldstein, and A. A. Alford, 2017: Improvements to the NOAA P-3 airborne Doppler tail-mounted radar: Super cell observations from VORTEX-Southeast. *38th Conf. on Radar Meteor.*, Chicago, IL, Amer. Meteor. Soc., 6A.2, https://ams.confex.com/ams/38RADAR/meetingapp.cgi/Paper/320666.

May, P. T., 2001: Mesocyclone and microburst signature distortion with dual PRT radars. *J. Atmos. Oceanic Technol.*, **18**, 1229–1233, https://doi.org/10.1175/1520-0426(2001)018<1229:MAMSDW>2.0.CO;2.

Miller, R. L., C. L. Ziegler, and M. I. Biggerstaff, 2020: Seven-Doppler radar and in situ analysis of the 25–26 June 2015 Kansas MCS during PECAN. *Mon. Wea. Rev.*, **148**, 211–240, https://doi.org/10.1175/MWR-D-19-0151.1.

Mitchell, E. D., S. V. Vasiloff, G. J. Stumpf, A. Witt, M. D. Eilts, J. T. Johnson, and K. W. Thomas, 1998: The National Severe Storms Laboratory Tornado Detection Algorithm. *Wea. Forecasting*, **13**, 352–366, https://doi.org/10.1175/1520-0434(1998)013<0352:TNSSLT>2.0.CO;2.

Montmerle, T., and C. Faccani, 2009: Mesoscale assimilation of radial velocities from Doppler radars in a preoperational framework. *Mon. Wea. Rev.*, **137**, 1939–1953, https://doi.org/10.1175/2008MWR2725.1.

NSSL, 2018: VORTEX Southeast. Accessed June 2018, https://www.nssl.noaa.gov/projects/vortexse/.

Oye, R. C., C. Mueller, and S. Smith, 1995: Software for radar translation, visualization, editing, and interpolation. *27th Conf. on Radar Meteorology*, Vail, CO, Amer. Meteor. Soc., 359–361.

Palucki, J. L., M. I. Biggerstaff, D. R. MacGorman, and T. Schuur, 2011: Comparison between low-flash and non-lightning-producing convective areas within a mature mesoscale convective system. *Wea. Forecasting*, **26**, 468–486, https://doi.org/10.1175/WAF-D-10-05012.1.

Savitzky, A., and M. J. E. Golay, 1964: Smoothing and differentiation of data by simplified least-squares procedures. *Anal. Chem.*, **36**, 1627–1639, https://doi.org/10.1021/ac60214a047.

Shen, F., J. Min, and D. Xu, 2016: Assimilation of radar radial velocity data with the WRF hybrid ETKF-3DVAR system for the prediction of Hurricane Ike (2008). *Atmos. Res.*, **169**, 127–138, https://doi.org/10.1016/j.atmosres.2015.09.019.

Sirmans, D., D. S. Zrnić, and B. Bumgarner, 1976: Extension of maximum unambiguous Doppler velocity by use of two sampling rates. *17th Conf. on Radar Meteorology*, Seattle, WA, Amer. Meteor. Soc., 23–28.

Skinner, P. S., C. C. Weiss, M. M. French, H. B. Bluestein, P. M. Markowski, and Y. P. Richardson, 2014: VORTEX2 observations of a low-level mesocyclone with multiple internal rear-flank downdraft momentum surges in the 18 May 2010 Dumas, Texas, supercell. *Mon. Wea. Rev.*, **142**, 2935–2960, https://doi.org/10.1175/MWR-D-13-00240.1.

Smith, T. M., and Coauthors, 2016: Multi-Radar Multi-Sensor (MRMS) severe weather and aviation products: Initial operating capabilities. *Bull. Amer. Meteor. Soc.*, **97**, 1617–1630, https://doi.org/10.1175/BAMS-D-14-00173.1.

Tabary, P., L. Perier, J. Gagneux, and J. Parent-Du-Chatelet, 2005: Test of a staggered PRT scheme for the French radar network. *J. Atmos. Oceanic Technol.*, **22**, 352–364, https://doi.org/10.1175/JTECH1709.1.

Torres, M. S., Y. F. Dubel, and D. S. Zrnić, 2004: Design, implementation, and demonstration of a staggered PRT algorithm for the WSR-88D. *J. Atmos. Oceanic Technol.*,

21, 1389–1399, https://doi.org/10.1175/1520-0426(2004)021 <1389:DIADOA>2.0.CO;2.

Vaisala, 2014: User's manual: Digital IF receiver/Doppler signal processer RVP8. Vaisala Doc., 391 pp., https:// usermanual.wiki/Baron-Services/XDD-1000C.S10- RECEIVER-AND-PROCESSOR-USERS-MANUAL- PART-1-374022.pdf.

——, 2017: User guide: RVP900 digital receiver and signal proc- esser. Vaisala Doc., 502 pp., ftp://ftp.sigmet.com/outgoing/ manuals/RVP900_Users_Manual.pdf.

Wurman, J., Y. Richardson, C. Alexander, S. Weygandt, and P. F. Zhang, 2007: Dual-Doppler analysis of winds and vorticity bud- get terms near a tornado. *Mon. Wea. Rev.*, **135**, 2392–2405, https://doi.org/10.1175/MWR3404.1.

——, D. Dowell, Y. Richardson, P. Markowski, E. Rasmussen, D. Burgess, L. Wicker, and H. B. Bluestein, 2012: The second Verification of the Origins of Rotation in Tornadoes Experi- ment: VORTEX2. *Bull. Amer. Meteor. Soc.*, **93**, 1147–1170, https://doi.org/10.1175/BAMS-D-11-00010.1.

Ziegler, C. L., E. N. Rasmussen, T. Shepherd, A. I. Watson, and J. M. Straka, 2001: The evolution of low-level rotation in the 29 May 1994 Newcastle–Graham, Texas, storm complex dur- ing VORTEX. *Mon. Wea. Rev.*, **129**, 1339–1368, https://doi. org/10.1175/1520-0493(2001)129<1339:TEOLLR>2.0.CO;2.

Zrnić, D. S., and P. Mahapatra, 1985: Two methods of ambiguity resolution in pulse Doppler weather radars. *IEEE Trans. Aerosp. Electron. Syst.*, **AES-21**, 470–483, 10.1109/TAES. 1985.310635.